

# DAS observations of perforation-induced guided waves in a shale reservoir

*Ariel Lellouch, Steve Horne, Mark Meadows, Stuart Farris, Tamas Nemeth, and Biondo Biondi*

## ABSTRACT

<sup>a</sup> Perforation shots can be recorded by downhole DAS arrays. In this study, we demonstrate that guided waves induced by perforation shots propagate in a low-impedance shale reservoir layer. Such guided waves have an extremely high frequency content of up to 700 Hz and are dispersive, with lower frequencies propagating faster than higher frequencies. They can propagate as both P- and S-waves, and their group velocity is higher than their phase velocity. The high temporal and spatial resolution of the DAS array allows for their unaliased recording despite their short wavelengths. The guided waves disappear from the records when the well exits the shale formation. Synthetic modeling predicts their existence for both the acoustic and elastic cases in simple velocity models. We also show that perforation shots from an offset well at a distance of 260 m can be recorded by the DAS array. Induced guided waves undergo significant disturbances when propagating through previously stimulated zones. These disturbances manifest as kinematic and dynamic changes of the recorded wavefield, and as scattered events. The nature of the stimulation-induced changes remains unresolved and their behavior is interpreted as a combination of unknown spatial and temporal effects. Guided waves hold tremendous potential for high-resolution reservoir imaging and should be used in conjunction with conventional DAS arrays and state-of-the-art DAS interrogators.

---

<sup>a</sup>The following is a minor variation of a The Leading Edge submission for a special section on borehole geophysics

## INTRODUCTION

Distributed acoustic sensing (DAS) is an emerging technology allowing for virtually continuous spatial and temporal recording of the seismic field by interrogating an optical fiber (Biondi et al., 2017; Lindsey et al., 2017; Mateeva et al., 2013). In addition, DAS can easily tolerate temperature and pressure regimes typically encountered in reservoirs and, therefore, does not prohibit downhole operations. DAS is being used for passive and active surveys in land as well as marine environments. Newly drilled boreholes are often instrumented with DAS fiber, allowing for multiple applications, such as vertical seismic profiling (VSP) surveys, microseismic monitoring, and low-

frequency strain measurements (Daley et al., 2016; Karrenbach et al., 2019; Mateeva et al., 2014).

Perforation shots have proven useful for velocity model calibration (Hogarth et al., 2017; Lellouch and Reshef, 2019; Maxwell, 2014). In this study, we analyze perforation shots recorded by a downhole DAS array. The fiber is installed behind casing along a deviated well drilled into an unconventional shale layer. This well is used for both DAS monitoring and production. Perforation shots are conducted along the horizontal part of the monitor well. We show that these shots generate waves that propagate through the subsurface, reaching distances of up to 1 km, depending on the source orientation. Through synthetic and field data analysis, we demonstrate that the low-impedance, strongly anisotropic shale formation acts as a waveguide for both P- and S- waves. The waveguide allows for the dispersive propagation of extremely high-frequency (up to 700 Hz) events. While guided waves have been previously observed in coal seams Buchanan (1976) and cross-well surveys Krohn (1992), downhole DAS allows for unprecedented resolution in the analysis of multiple wave types.

In addition, we analyze perforation shots excited from an offset horizontal well located roughly 260 m away from the monitor well. Events are reliably recorded at offsets of more than 600 m. Since perforations are part of a stimulation program, we can observe propagation differences of P- and S- guided waves between stimulated and undisturbed parts of the shale reservoir. This study sets the stage for high-resolution mapping of fractured reservoirs.

## SUBSURFACE PROPERTIES AND ACQUISITION GEOMETRY

In this study area a deviated well was drilled into an unconventional shale formation. In Figure 1(a), we show a side view of the well trajectory. The horizontal part of the well spans over 1.5 km. In addition, we show results of vertical logging in a nearby well. Depths have been manually adjusted. The shale formation is visible in all logs. It is about 15 m thick and located at depths of roughly 1.97 to 1.985 km at the vertical well location. In Figure 1(b), we show logging results recorded in the horizontal part of the well. They display relatively small lateral variation, indicative of the layered geology of the area. In addition, their analysis shows that the well does not break out of the shale formation at any location, which is confirmed by completion logs. Finally, the significant shear-wave splitting seen in Figure 1(b) indicates strong anisotropy. As a consequence of the layered geology and shale behavior (Sayers, 2005), a vertically transverse isotropy (VTI) approximation of the anisotropic shale is reasonable for this area. The difference between the vertical P-wave velocity (Figure 1a, in red) and the horizontal P-wave velocity (Figure 1b, in red) is substantial, also indicating the strongly anisotropic nature of the shale layer.

The well has been instrumented with DAS fiber cemented behind casing and spans a total distance of almost 4 km from the wellhead to the toe (end of the well). The

fiber was interrogated using the Silixa iDAS system, with a channel spacing of 1 m, gauge length of 10 m, and a sampling frequency of 2 kHz. Data are acquired as strain-rate along the direction of the fiber. Perforation shots are generated as part of a stimulation program. There are 31 stimulation stages along the horizontal part of the DAS-instrumented monitor well, each comprising 5 or 6 perforation shots. Stages start at the toe and are nearly uniformly spaced along the well. The average distance between shots is 10 m. Shots are directional and activated 180 degrees away from the fiber.

## RECORDED PERFORATION SHOT

In Figure 2(a), we show a perforation shot initiated roughly 600 m from the toe and associated one-sided propagation towards the heel (the bent part of the well) in the undisturbed area of the reservoir. Different perforation shots are very similar to each other and display the same behavior. We apply a velocity band-pass filter of 2500-5000 m/s. The F-K analysis of these data is shown in Figure 2(b). There are two types of waves in this record, discernable in both plots: guided waves and head waves. The head wave propagates up to distances of 300 m; it has a frequency content of up to 250 Hz and a velocity that matches that of the shale layer above. There are no clear signs of a head wave from below the shale layer, which has a significantly higher velocity ( $> 5.5 \text{ km/s}$ ) and impedance contrast than the layer above (see Figure 1(a)). The guided waves propagate to longer distances (500 m) than the head wave and have a wide frequency content up to 700 Hz. They are dispersive, with the lower frequencies propagating faster than the higher ones. This can be observed in both temporal records (a) and their F-K spectrum (b). The lower frequencies generally lie above the dotted line in (b), while the higher frequencies are below it. In addition, for all frequencies, the phase velocity ( $f/k$ ) is higher than the group velocity ( $\partial f / \partial k$ ), as expected. As a rough estimate, the phase velocities are higher by about 10% – 15%, depending on the frequency.

## SYNTHETIC EXAMPLE ACOUSTIC PROPAGATION

In this section, we confirm the existence of guided waves in a simplified acoustic scenario. Figure 3(a) contains a summary of the synthetic setup. Due to the strong anisotropy of the shale layer, logging velocities have to be adjusted to reasonably match actual propagation velocities. We use the vertical logs to build a 1-D profile of the P-wave velocity. With such a structure, it is possible to model both the vertical/deviated and the horizontal parts of the well in the same medium. Naturally, in reality, the horizontal part is simply a continuation of the deviated one. Values above and below the shale layer are coarsely blocked with constant values. Within the shale area, indicated by high-gamma ray values, we scale the velocities and retain the original log variations. After scaling, velocities should be close to the average horizontal log velocity. Due to the strong anisotropy of the shale reservoir, such

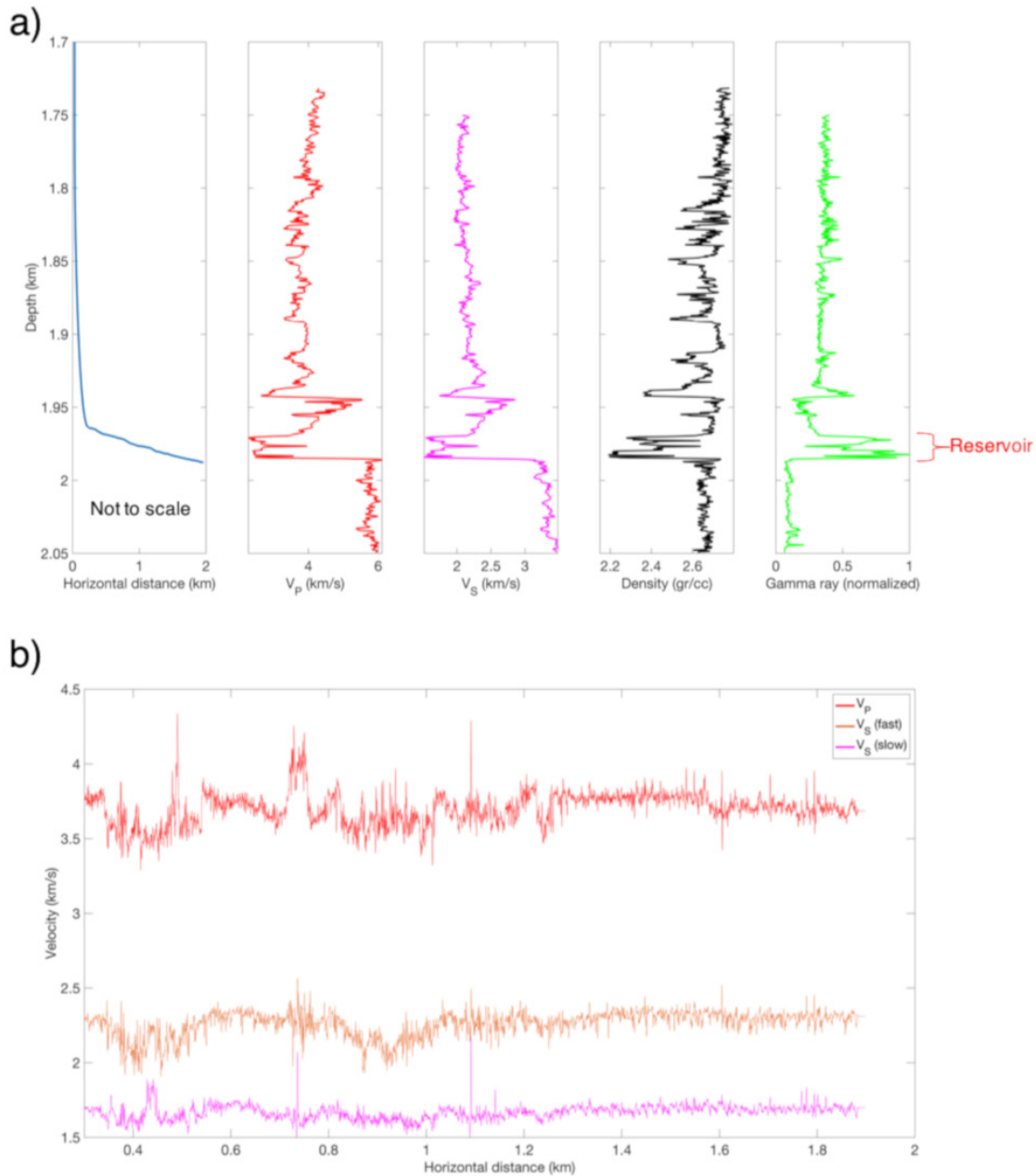


Figure 1: (a) Monitor well trajectory (blue) and vertical logging results from a nearby well. Axes are not to scale. We show P- (red) and S- (magenta) wave velocity, density (black) and normalized gamma-ray (green) logs. The shale layer, denoted by a red brace, is located at depths of 1.97 to 1.985 km and is characterized by low velocities, low density, and high gamma-ray values. (b) Horizontal logs for  $V_P$ , fast  $V_S$ , and slow  $V_S$  in the monitor well. Velocities vary slightly with distance and are nearly constant for the last 900 m. The noticeable discrepancy between fast and slow  $V_S$  is associated with significant shear-wave splitting, indicative of strong anisotropy. [NR]

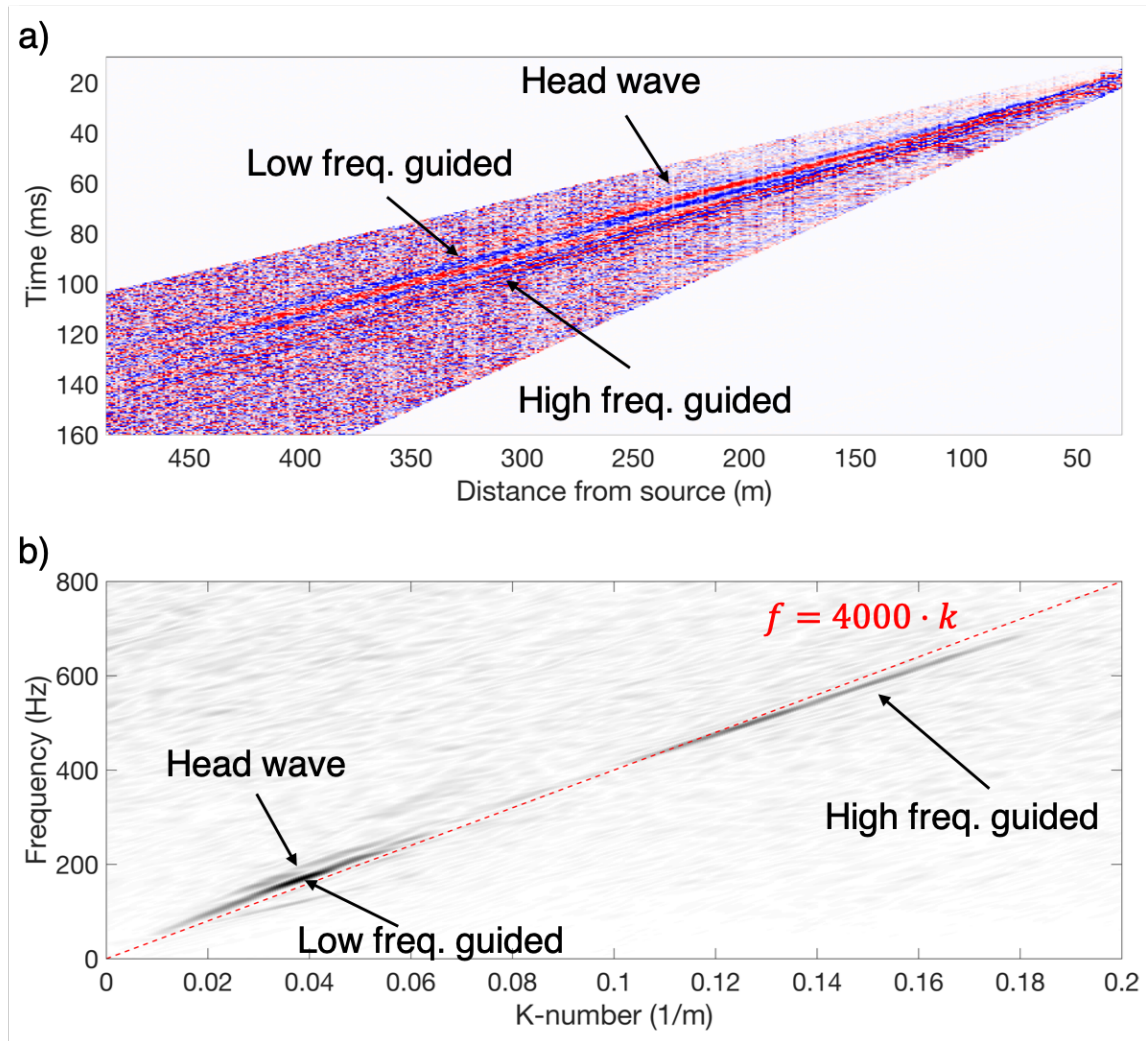


Figure 2: (a) One-sided propagation of perforation shot and (b) its F-K spectrum. In (b), a linear frequency-wavenumber relation with a propagation velocity of 4 km/s is shown for reference (red dotted line). Events of interest are denoted by black arrows. The shot excites guided waves, which can be seen up to distances of 500 m away from the source. They have an extremely high frequency content, reaching close to 700 Hz. Such waves are dispersive, with the lower frequencies propagating faster than the higher ones. In addition, a higher-velocity head wave can also be observed, which propagates shorter distances and with a lower frequency content than the guided waves, and with a velocity that matches that of the shale layer above. [NR]

scaling amounts to a 30–40% increase of the P-wave log velocity. As the guided waves propagate mostly horizontally in the shale layer, this is a reasonable compromise. Density logs are used directly. Modeled data are shown in Figure 3(b), and their F-K analysis in Figure 3(c). Data are converted to their strain-rate equivalent by taking a combination of their spatial and temporal derivatives and subsequently applying a spatial filter emulating the 10 m gauge length with which the field data are recorded. For simplicity, we use a rectangular filter, which is only a coarse approximation. Finally, a band-pass filter is applied to match the frequencies of the field data.

We are able to recreate the behavior of guided waves even with this simple acoustic model. The dispersion behavior is similar to what we see in the field data records. However, we observe only a single guided mode in the field data, whereas in the synthetic data, higher-order modes are also present. It is also worth noting that frequency notches are introduced by the gauge-length effect (Dean et al., 2017). Field data also appear to have such notches at the same wavenumbers observed in the synthetic data. A second difference is that the head wave from the top of the layer is absent in the modeled data. We show below that such a head wave arises when elastic modeling is conducted. For a more intuitive understanding of the propagation mechanism, we show two snapshots of the full wavefield in Figure 4. The waveguide nature of the shale layer is clearly evident. In addition, Figure 4 shows the weakness of the head waves when recorded by an array located within the shale layer.

## RECORDING IN THE NON-HORIZONTAL SECTION OF THE WELL

In Figure 5, we show records of a perforation shot close to the heel of the well. This shot is recorded by both the horizontal (right side) and vertical/heel (left side) parts of the DAS array. We compare the recorded field data (Figure 5(b)) with synthetic seismograms (Figure 5(a)). The depth of the well at different locations is plotted on top of the recorded data. The synthetic wavefield is displayed at the locations at which field data were acquired. Distances from the source are computed as Euclidean distance between source and receivers and do not take into account true propagation paths in the vertical/heel part. In both field and synthetic datasets, the guided waves disappear when the well exits the shale formation. This reconfirms that the existence of these waves is limited to the low-impedance areas only within the shale layer. Outside this area, only body waves can propagate. In addition, both records show a clear moveout change when the well exits the shale layer. As the waves continue propagating to the left, they encounter a higher velocity than do guided waves propagating to the right, and they increase in amplitude. This is expected, as propagation outside the shale layer is that of body waves within a faster medium. After analyzing the data from all available perforation shots, we did not see any area within the horizontal section in which the guided waves disappear. This is confirmed by the completion log, according to which the well did not break formation at any location.

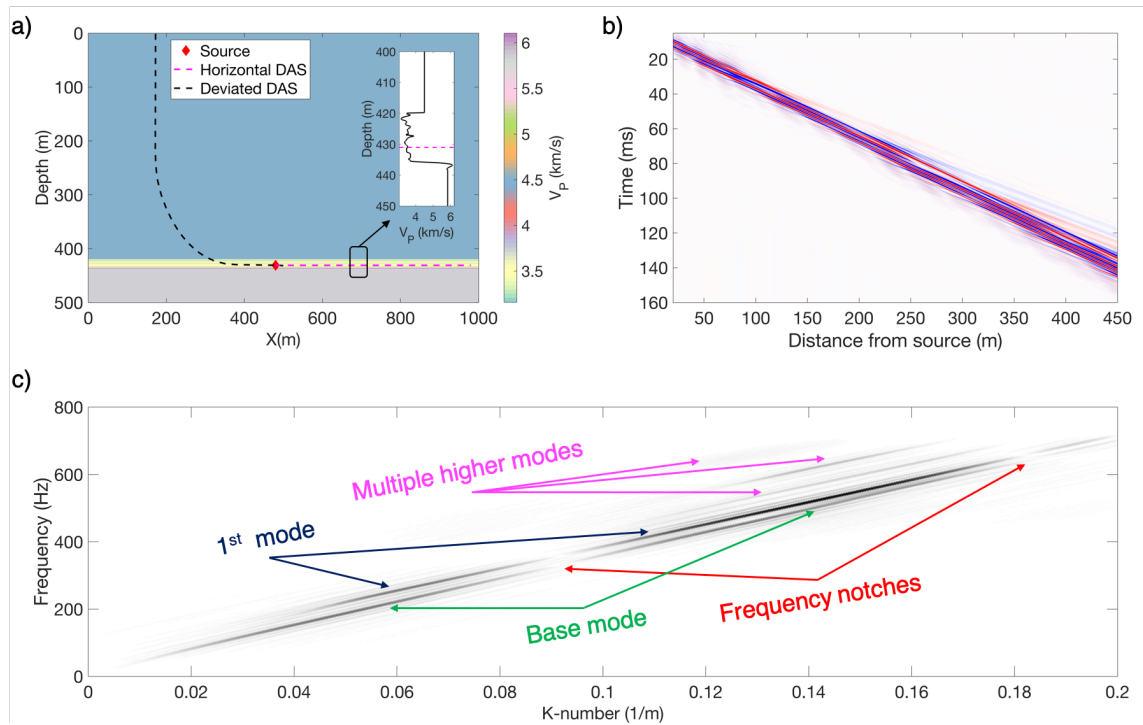


Figure 3: (a) Synthetic example setup. The 1-D velocity model is shown in the inset, along with a zoomed-in version around the shale reservoir. Velocities above and below the shale are constant. The source is denoted by a red diamond. There are two acquisition setups horizontal (magenta line) and deviated (black line). The latter follows the true well trajectory near the heel. (b) Data modeled for horizontal DAS recording and (c) its F-K spectrum. Events of interest are denoted by arrows of different colors. [NR]

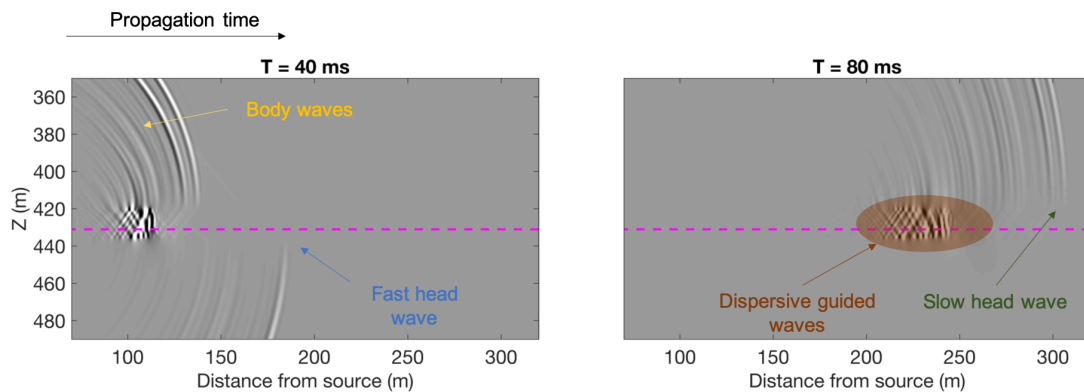


Figure 4: Two snapshots of recorded acoustic data (prior to conversion to strain-rate) at 40 ms and 80 ms after source activation, zoomed in on the shale layer. The dashed magenta line indicates the location of the horizontal recording array. We denote body waves (yellow), head waves (fast blue, slow green) and the dispersive guided waves (brown). [NR]

The field data display significant S-waves in the vertical/heel part. Their prominence is due to the fiber directivity, which is more sensitive to S-wave polarizations in this geometrical setup (Martin et al., 2018). The S-waves appear to follow a different moveout pattern than do the P-waves, indicating variable  $V_P/V_S$ , as can be confirmed by the vertical logs (Figure 1). Of course, the acoustic modeling results in Figures 3, 4, 5 do not contain S-waves, providing motivation for a further modeling study with elastic wave propagation.

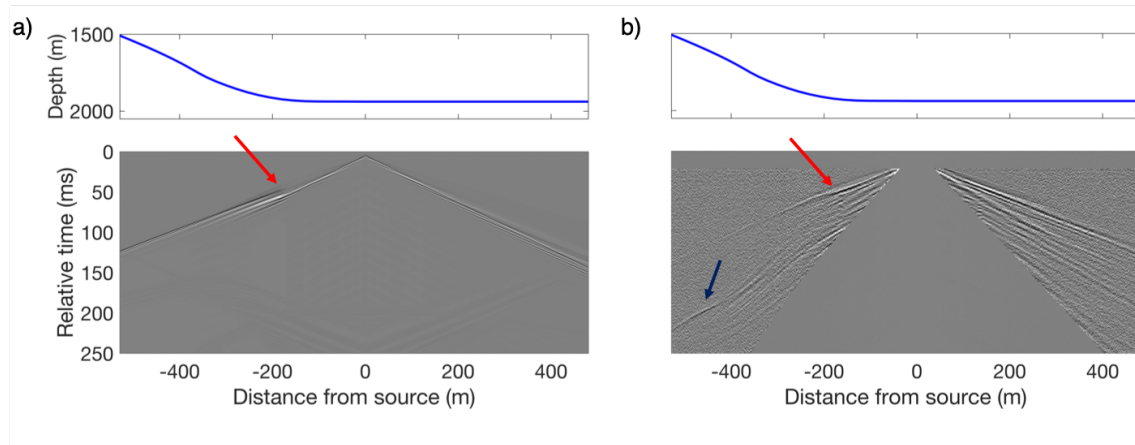


Figure 5: Synthetic (a) and field (b) records close to the heel of the well. The well depth at each location is displayed on top of the recorded data. Seismograms are ordered by signed distance and computed as 2-D Euclidean source-receiver distance. At the location of the bend in the well (red arrows), the guided waves disappear, and first arrivals undergo a clear moveout change. Propagation outside the shale reservoir is faster, as expected. For the field data record, S-waves are clearly visible in the heel/vertical part of the well (dark blue arrow). [NR]

## SYNTHETIC EXAMPLE - ELASTIC PROPAGATION

In the field data, S-waves are significantly weaker than P-waves. In addition, they appear clearly only for certain shots. We recompute 2-D synthetic seismograms for a horizontal acquisition geometry using the elastic wave equation. The perforation shot is modeled as a force stress source directed along the Z-axis, perpendicular to the horizontal array. Data are extracted as displacements in the X-axis direction and converted to strain-rate equivalents. Construction of the S-wave velocity model is similar to the P-wave modeling workflow discussed earlier, but scaling is performed to match the fast S-waves. As a result, if guided waves can propagate in such a model, they will exist for the slower S-waves as well.

Modeled data and their F-K analysis are shown in Figure 6. The head wave arising from the P-waves can now be clearly seen, in accordance with the field-data records. There is an S head wave as well, propagating at the shear velocity of the medium below the shale. Both head waves propagate for short distances, as is the case for

the field data. Both P- and S- guided waves propagate with a dispersive behavior containing multiple modes, as in the acoustic case. As before, slower frequencies propagate faster than high frequencies, and the phase velocity is higher than the group velocity. It is worth mentioning that there are no clear conversions between P- and S- waves. If there were, converted events should have a moveout intermediate between that of the P- and S- waves, but that area in the F-K domain remains empty. Guided waves propagate with supercritical angles in the shale layer. At such angles (above 70 degrees), the Zoeppritz equations (Aki and Richards, 2002) predict very small conversion coefficients. Naturally, the complexity of the subsurface may add other degrees of freedom and a frequency-dependent behavior.

In contrast to the modeling results, P-waves are stronger in the field data. In addition, S-waves are only visible for some of the perforation shots. However, this effect might be due to a combination of the source orientation, mechanism, and fiber directivity. We model a very simplistic directional force in a 2-D setup, which does not capture the complexities of a real perforation shot. Nevertheless, the synthetic results show that the shale layer can sustain guided S-waves.

## RECORDING OF PERFORATION SHOTS FROM A PARALLEL WELL

Perforation shots were also excited in a nearby offset well and recorded by the monitor well. The horizontal sections of the wells are parallel and separated by a distance of 260 m. The perforation shots are part of a stimulation program, going from toe to heel and separated into stages. Each stage is comprised of 5 perforation shots, spaced roughly 10 m apart. The distance between stages is about 50 m and there is a 6-to-8-hour delay between consecutive stages. As a result, for each recorded shot we can observe propagation through previously stimulated zones (towards the toe) as well as undisturbed ones (towards the heel).

In Figure 7, we show the analysis of a perforation shot located roughly 500 m from the toe. The recorded data display both P- and S- guided waves, with the previously observed dispersion effect of faster propagation at the lower frequencies. A reasonable approximation of the travel times for a given frequency component can be obtained with a constant-velocity approximation, which is strong evidence of the 1-D nature of the velocity structure. The S-wave velocity indicates that propagation corresponds to the fast S mode (see Figure 1), or SH mode in the case of VTI anisotropy. Data undergo offset binning with a 0.25 m resolution in order to create a uniformly sampled version of the data for F-K analysis. The frequency content is again very high and reaches up to 700 Hz for the P-waves and 600 Hz for the S-waves. The F-K analysis also shows that, as before, phase velocities are higher than group velocities for all frequencies. In contrast to perforation shots excited in the monitor well, the S-waves here are stronger than the P-waves. This validates the elastic synthetic example, showing that the geological structure can sustain strong S-wave guided modes.

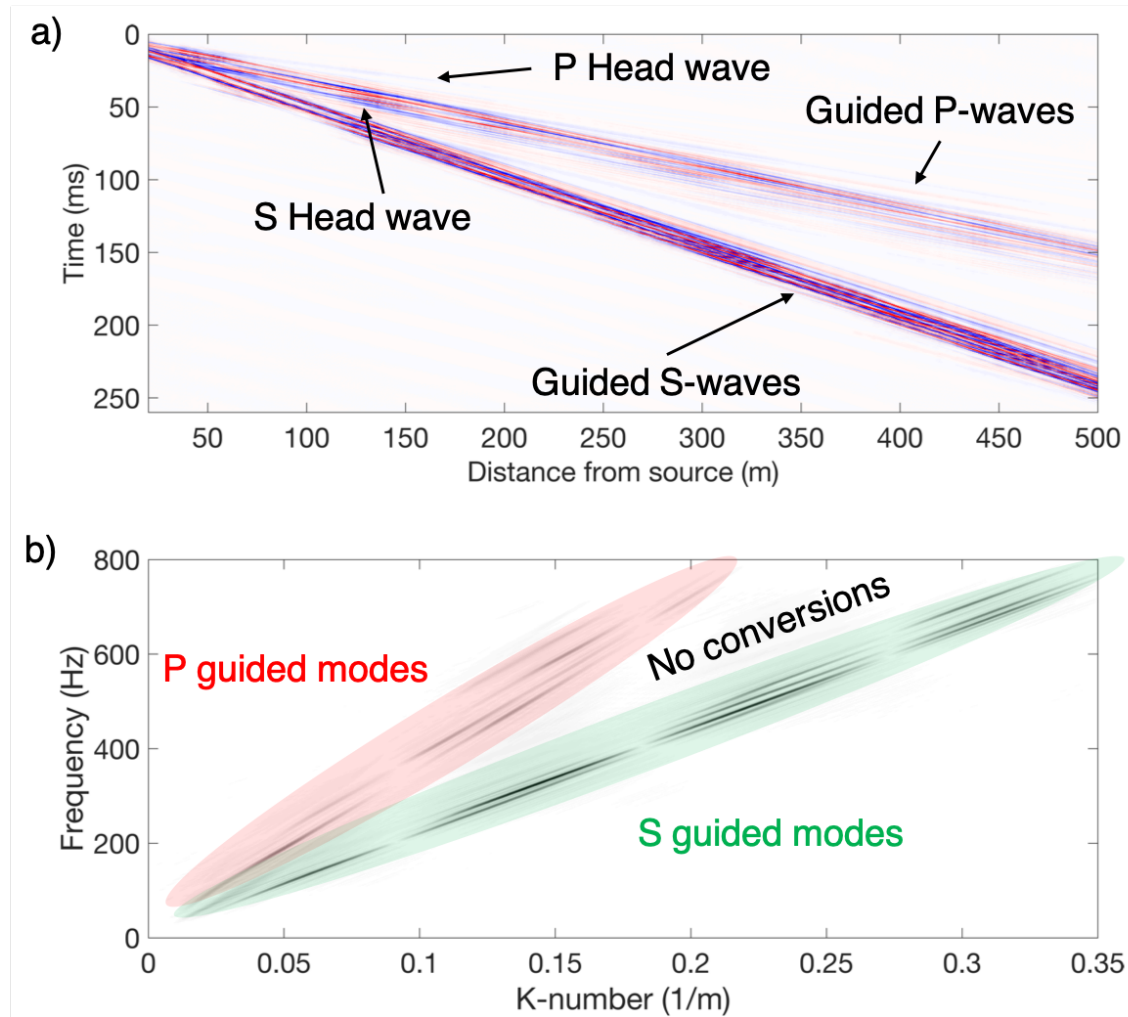


Figure 6: Elastic modeling for horizontal acquisition. Recorded data are in (a) and their F-K analysis is in (b). The P head wave from the top of the layer is visible and denoted by an arrow. In addition, the S head wave is also visible. Also shown are P- and S- waves that propagate as dispersive guided waves, containing multiple modes. They are denoted in red and green, respectively, in (b). Note that guided S-waves are stronger than guided P-waves. Interestingly, there do not seem to be any propagating PS / SP converted modes. If they existed, they would appear between the P and S modes, roughly where No conversions is marked in the F-K domain. [NR]

We also observe obvious propagation differences in the previously stimulated and undisturbed part of the shale reservoir. In the stimulated area, S-waves induce a strong scattered event, visible along a wide portion of the DAS array. The P arrivals also induce such an event, originating at the same spatial location, but it is much weaker. For many perforation shots, the P-induced scattering is invisible, and the S-induced scattering is less obvious than in the shot displayed in Figure 7. However, regarding the S-waves, there is a clear disturbance in the propagation of the guided waves, and the record is asymmetric. This property is true for all the shots we observed. As all these observations spatially coincide, we conclude that there is a subsurface heterogeneity at that location, probably created by a previous stimulation.

In Figure 8, we show a different type of analysis. We observe a 200-m section of DAS channels recording perforation shots from different locations.  $H$  indicates the horizontal distance between shot locations and the center of the common subsurface location that is being analyzed. This is a form of common-receiver gather. It is important to remember that there is also a significant time difference between shots, as stages are separated 6-8 hours apart. A single shot was chosen from each stage. Propagation in the undisturbed part ( $H = 289$  m,  $210$  m and  $92$  m) appears continuous and smooth for both P and S events. The perforation shots almost directly in front of the array ( $H=5$  m) appear disturbed in both P and S arrivals. We can also observe a polarity flip due to the fiber directivity. For  $H= -20$  m, both phases appear disturbed, even though the S is more affected. For propagation in the disturbed part at intermediate distances ( $H= -107$  m,  $-144$  m) we see a very interesting phenomenon. The P arrivals appear practically unaffected, whereas the S-waves are strongly disturbed. In addition, the S-waves appear to generate some scattered energy, propagating in the opposite direction. For  $H= -214$  m, there is no visible scattering, but the propagation is affected for the rightmost part of the array. At a longer distance ( $H = -271$  m) the wavefront propagation reverts to its normal, unaffected state.

## DISCUSSION

The temporal and spatial resolution offered by DAS systems allows for an unprecedented recording of high-frequency guided waves. Their spatial wavelength can be as short as 5 m for P-waves and 3 m for S-waves. No feasible conventional acquisition system could sample such wavelengths over a wide range of angles without strongly aliasing them. The wide frequency content of these guided waves confirms the need for temporal sampling at 2 kHz and above. However, in this study the acquisition used a gauge length of 10 m, which interfered with the recorded signal. Newer DAS systems can offer shorter gauge lengths without compromising the signal-to-noise ratio. From this study, it seems that a reduction of the gauge length to 2 or 3 m would be beneficial, especially for S-waves.

Perforation shots from offset wells appear very promising for detecting, inverting and imaging fracture zones. The reason is that the clearest difference in propagation appears in the S-waves. The greater sensitivity of S-waves to fractures relative to P-

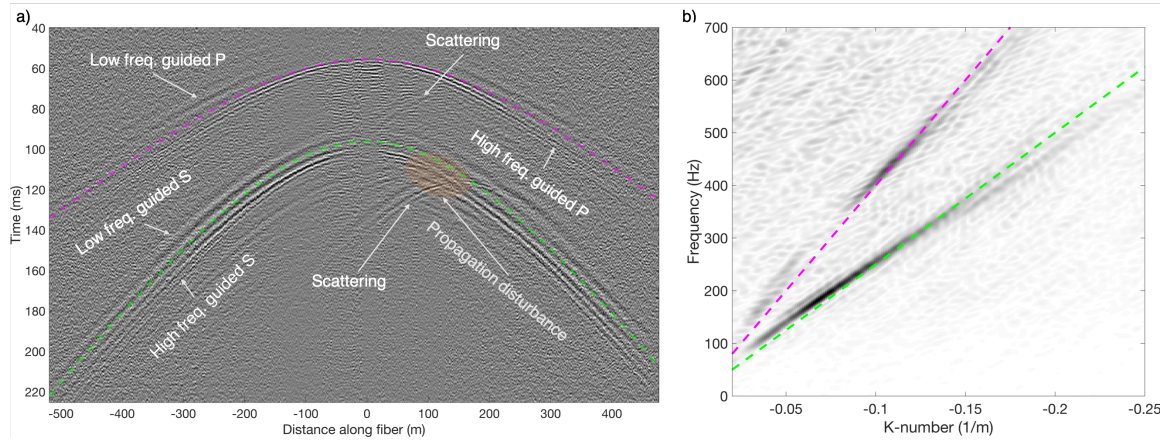


Figure 7: Perforation shot from an offset well (a). Recorded traces are ordered by 1-D signed horizontal distance from the estimated source location. Positive distances (right) indicate propagation in the direction of a previously stimulated area. Hyperbolic moveouts, computed with  $V_P = 4 \text{ km/s}$  (magenta) and  $V_S = 2.5 \text{ km/s}$  (green), are overlaid on recorded data. The absolute timing of the shot is unknown, and the time axis is arbitrary. The dispersive nature of both P- and S- waves is clearly visible, as low frequencies propagate faster than higher ones. In addition, we observe a propagation disturbance for the S-waves in the previously stimulated zone (orange ellipse). There is also a scattered event originating at the same location. Such scattering is also present for the P-waves, despite being significantly weaker. (b) F-K analysis of undisturbed propagation (left side only). Two  $f = c \cdot k$  lines are plotted, with  $c=4 \text{ km/s}$  (magenta, for P) and  $c=2.5 \text{ km/s}$  (green, for S). [NR]

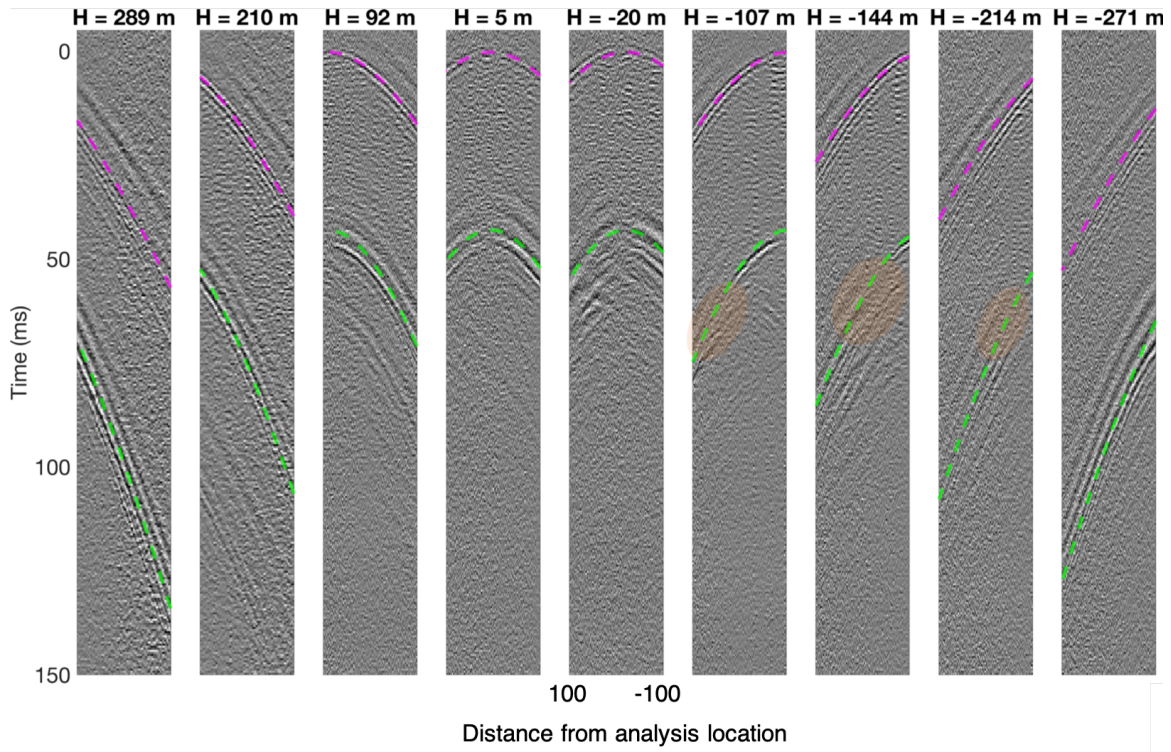


Figure 8: Common-receiver area analysis of different perforation shots. A fixed portion of the DAS array, 200 m wide, recording different perforation shots is displayed. The horizontal 1-D distance between the center of the recording array and the estimated shot location ( $H$ ) is plotted at the top. Positive distances indicate that the wavefields are propagating in an undisturbed area, whereas negative distances specify a previously stimulated zone. Hyperbolic moveouts, computed with  $V_P = 3.7 \text{ km/s}$  (magenta) and  $V_S = 2.3 \text{ km/s}$  (green), are overlaid on recorded data. As the absolute timing of the shot is unknown, the time axis has been manually adjusted. Areas of disturbed S-wave propagation in which P-waves appear as weakly or not affected are marked with ellipses. [NR]

waves is a well-known phenomenon (Schoenberg and Sayers, 1995). The fact that S-waves are more easily recorded by DAS fiber in wells adjacent to the treated well than in the treated well itself is due to the more favorable geometry of obliquely incident S-wave polarizations arriving from the offset well. For the same reason, perforation shots excited in the monitor well appear to generate much weaker recorded S-wave energy, and the existence of such waves is less consistent from shot to shot. When perforations are recorded from an offset well, however, S-waves are dominant, and changes in their character can be easily detected. Unquestionably, stimulation induces changes in the subsurface, but some uncertainty remains regarding the effect of such changes on the time-dependent S-wave behavior. When sources are far enough ( $> 300m$ ) from the analyzed area, the wavefronts behave as if propagating in an undisturbed medium. This can be explained by two different mechanisms, possibly in combination. The first is that induced fractures close down and the surrounding matrix returns to its original state (Karrenbach et al., 2019) after a relatively short period, usually over a few hours Meadows and Winterstein (1994), whereas the total stimulation time period covered in this study is over several days. The second possible cause is purely spatial, for cases where the extent of the fractures that propagate towards the monitor well is limited. As a result, waves excited at larger distances from the monitor well simply do not cross the undisturbed areas.

## CONCLUSIONS

We show the existence, using field and synthetic data, of P- and S- guided waves induced by perforation shots and propagating in a shale reservoir. They disappear when the well exits the formation. These waves are excited whether the perforation shot is conducted in the monitor well or in an offset well. However, the relative strength of P- and S- waves, both of which can propagate in the low-impedance shale layer, varies between the two cases. Guided waves have a very high frequency content (up to 700 Hz) and can only be sampled thanks to the spatial and temporal resolution of the DAS array. They are dispersive, with slower frequencies propagating faster than higher ones, and with phase velocities that exceed group velocities, as expected. By studying perforation shots induced from an offset well, we observe noticeable propagation disturbances in wavefields traveling through stimulated zones. The effect of the induced fractures on S-waves is significant, while in most cases P-waves propagate weakly, if at all, disturbed. The short wavelengths of the guided waves make them an ideal candidate for high-resolution mapping of fractured reservoirs. We thus strongly advocate for the utilization of guided waves in conjunction with state-of-the-art DAS systems in further studies of such areas.

## ACKNOWLEDGEMENT

We are thankful to Chevron Energy Technology Company for providing recorded data, logs, additional information relevant to this study, and the permission to publish this

study. We personally thank Mike Craven and Dimitri Bevc for their helpful comments and discussions.

## REFERENCES

- Aki, K. and P. G. Richards, 2002, *Quantitative Seismology*. Geology (University Science Books): Seismology: University Science Books.
- Biondi, B., E. Martin, S. Cole, M. Karrenbach, and N. Lindsey, 2017, Earthquakes analysis using data recorded by the Stanford DAS Array: SEG Technical Program Expanded Abstracts, 2752–2756.
- Buchanan, D. J., 1976, The propagation of attenuated SH channel waves: *Geophysical Prospecting*, **26**, 16–28.
- Daley, T. M., D. E. Miller, K. Dodds, P. Cook, and B. M. Freifeld, 2016, Field testing of modular borehole monitoring with simultaneous distributed acoustic sensing and geophone vertical seismic profiles at Citronelle, Alabama: *Geophysical Prospecting*, **64**, 1318–1334.
- Dean, T., T. Cuny, and A. H. Hartog, 2017, The effect of gauge length on axially incident P-waves measured using fibre optic distributed vibration sensing: *Geophysical Prospecting*, **65**, 184–193.
- Hogarth, L. J., C. M. Kolb, and J. H. Le Calvez, 2017, Controlled-source velocity calibration for real-time downhole microseismic monitoring: *The Leading Edge*, **36**, 172–178.
- Karrenbach, M., S. Cole, A. Ridge, K. Boone, D. Kahn, J. Rich, K. Silver, and D. Langton, 2019, DAS microseismic, strain and temperature monitoring during hydraulic fracturing: *Geophysics*, **84**, D11–D23.
- Krohn, C. E., 1992, Crosswell continuity logging using guided seismic waves: *The Leading Edge*, **11**, 39–45.
- Lellouch, A. and M. Reshef, 2019, Velocity analysis and subsurface source location improvement using moveout-corrected gathers: *Geophysics*, **84**, KS119–KS131.
- Lindsey, N. J., E. R. Martin, D. S. Dreger, B. Freifeld, S. Cole, S. R. James, B. L. Biondi, and J. B. Ajo-Franklin, 2017, Fiber-Optic Network Observations of Earthquake Wavefields: *Geophysical Research Letters*, **44**, 792–799.
- Martin, E. R., N. J. Lindsey, and B. Biondi, 2018, Introduction to Interferometry of Fiber Optic Strain Measurements: *EarthArXiv*, **14 June**, 1–33.
- Mateeva, A., J. Lopez, J. Mestayer, P. Wills, B. Cox, D. Kiyashchenko, Z. Yang, W. Berlang, R. Detomo, and S. Grandi, 2013, Distributed acoustic sensing for reservoir monitoring with VSP: *The Leading Edge*, **32**, 3–7.
- Mateeva, A., J. Lopez, H. Potters, J. Mestayer, B. Cox, D. Kiyashchenko, P. Wills, S. Grandi, K. Hornman, B. Kuvshinov, W. Berlang, Z. Yang, and R. Detomo, 2014, Distributed acoustic sensing for reservoir monitoring with vertical seismic profiling: *Geophysical Prospecting*, **62**, 679–692.
- Maxwell, S., 2014, *Microseismic Imaging of Hydraulic Fracturing: Improved Engineering of Unconventional Shale Reservoirs*: SEG Distinguished Instructor Series No. 17.

- Meadows, M. A. and D. F. Winterstein, 1994, Seismic detection of a hydraulic fracture from shear-wave VSP data at Lost Hills Field , California: *Geophysics*, **59**, 11–26.
- Sayers, C. M., 2005, Seismic anisotropy of shales: *Geophysical Prospecting*, **53**, 667–676.
- Schoenberg, M. and C. M. Sayers, 1995, Seismic anisotropy of fractured rock: *Geophysics*, **60**, 204–211.